ON THE FLOW PAST A CIRCULAR CYLINDER FROM CRITICAL TO SUPER-CRITICAL REYNOLDS NUMBERS: WAKE TOPOLOGY AND VORTEX SHEDDING

I. Rodríguez[1], *O. Lehmkuhl*[1,2], *J. Chiva*[1], *R. Borrell*[2] *and A. Oliva*

[1] *Heat and Mass Transfer Technological Center (CTTC), Universitat Politècnica de Catalunya -BarcelonaTech. Colom 11 08222 Terrassa, Spain*
[2] *TermoFluids S.L, Av. Jacquard 97 08222, Barcelona, Spain*
cttc@cttc.upc.edu

Abstract

The flow past a circular cylinder at critical and supercritical Reynolds number combines flow separation, turbulence transition, reattachment of the flow and further turbulent separation of the boundary layer. The transition to turbulence causes the delaying of the separation point and, an important reduction of the drag force on the cylinder surface. In the present work, large-eddy simulations of the flow past a circular cylinder at Reynolds numbers in the range 2.5×10^5-8.5×10^5 are performed. In this range, major changes in the pressure distribution occur, the pressure minimum gets more negative as its location moves towards the cylinder rear, whereas the base pressure increases. These changes are shown to take place first on one side of the cylinder and then on the other side as the drag completes its drop up to a minimum value of $\sim$0.23, registered at $Re = 6.5 \times 10^5$ in this work. After that, the flow enters in the supercritical regime, with little changes in the wake configuration. Furthermore, these changes in the wake topology as the Reynolds number increases are also shown to be related to the increase in the vortex shedding frequency.

1 Introduction

It is well known that the wake topology in the flow past a circular cylinder remains almost unchanged up to Reynolds number $\sim 10^5$ (Williamson, 1996). Then, at $Re \sim 2 \times 10^5$ major changes take place entailing flow separation, turbulence transition in the detached shear layers, reattachment of the flow and further separation of the boundary layer. Furthermore, a dramatic decrease in the drag coefficient occurs between Reynolds numbers 2×10^5 and 5×10^5. In this regime, transition to turbulence first occurs in one of the boundary layers and it is characterized by the separation with further reattachment of the boundary layer, forming a bubble similar to that observed in the flow past airfoils at low-to-moderate Reynolds numbers. This laminar separation bubble (LSB) on one side of the cylinder surface is the cause of asymmetric forces acting on the cylinder surface with the mean lift coefficient greater than zero ($C_L > 0$) (Bearman, 1965; Schewe, 1983).

In the super-critical regime ($Re = 5 \times 10^5 - 2 \times 10^6$), two LSB on both sides of the cylinder surface are observed. Furthermore, there is a plateau in the value of the drag coefficient ($C_D \approx 0.2$) and turbulent boundary layer separation occurs at $\phi = 148°$ on both sides of the cylinder (Delany and Sorensen, 1953; Achenbach, 1968; Shih et al., 1993). The wake is thinner than in the subcritical regime, with width lower than the cylinder diameter. A point of controversy is the existence of vortex shedding at these Reynolds numbers. In fact, few measurements of vortex shedding frequency are reported with a considerable scattering (Delany and Sorensen, 1953; Bearman, 1969; Achenbach and Heinecke, 1981; Schewe, 1983). These results contrast with other works which claim that in this regime there is not vortex shedding whatsoever (Roshko, 1961; Van Nunen, 1974; Shih et al., 1993).

Up-until-now, time accurate numerical simulations of the turbulent flow past a circular cylinder have been limited to low-to-moderate Reynolds numbers (see for instance Dong et al. (2006), Lehmkuhl et al. (2013)). So far, due to limitations of the computational resources, numerical simulations of the flow in the critical regime are scarce. Breuer (2000) performed challenging LES at the subcritical Reynolds number of $Re = 1.4 \times 10^5$ and later, Catalano et al. (2003) used LES with wall-modeling at super-critical Reynolds numbers of 5×10^5, 10^6 and 2×10^6. More recently, Moussaed et al. (2014) used a blending of a variational multi-scale LES (VMS-LES) with a RANS model for simulating the super-critical regime at $Re = 6.5 \times 10^5 - 1.25 \times 10^6$.

In this work large-eddy simulations of the flow at critical and super-critical Reynolds numbers in the range of $Re = U_{ref}\, D/\nu = 2.5 \times 10^5 - 8.5 \times 10^5$ are carried out. These simulations aim at shedding some light into the changes in topology which occur at these Reynolds numbers and to answer the question whether vortex shedding is suppressed at supercritical Reynolds numbers.

2 Mathematical and numerical model

The spatially filtered Navier-Stokes equations can be written as,

$$\frac{\partial \overline{u}_i}{\partial t} = 0 \quad (1)$$

$$\frac{\partial \overline{u}_i}{\partial t} + \frac{\partial \overline{u}_i \overline{u}_j}{\partial x_j} - \nu \frac{\partial^2 \overline{u}_i}{\partial x_j \partial x_j} + \rho^{-1} \frac{\partial \overline{p}}{\partial x_i} = -\frac{\partial \mathcal{T}_{ij}}{\partial x_j} \quad (2)$$

where $\overline{u}$ and $\overline{p}$ stand for the filtered velocity and pressure, respectively. ν is the kinematic viscosity and ρ the density of the fluid. In the equation 2, $\mathcal{T}_{ij}$ is the subgrid scale (SGS) stress tensor which has to be modelled. Its deviatoric part is given by,

$$\mathcal{T}_{ij} - \frac{1}{3}\mathcal{T}_{kk}\delta_{ij} = -2\nu_{sgs}\overline{\mathcal{S}}_{ij} \quad (3)$$

where $\overline{\mathcal{S}}_{ij}$ is the large-scale rate-of-strain tensor, $\overline{\mathcal{S}}_{ij} = \frac{1}{2}\left(g_{ij} + g_{ji}\right)$ being $g_{ij} = \partial \overline{u}_i / \partial x_j$. δ_{ij} is the Kronecker delta. To close the formulation, an appropriate expression for the subgrid-scale viscosity should be provided. In this paper, the wall-adapting local-eddy viscosity model (WALE) (Nicoud and Ducros, 1999) is used. The WALE model evaluates the eddy viscosity as,

$$\nu_{sgs} = (\mathcal{C}_w \Delta)^2 \frac{(\overline{\mathcal{V}_{ij}} : \overline{\mathcal{V}_{ij}})^{\frac{3}{2}}}{(\overline{\mathcal{S}_{ij}} : \overline{\mathcal{S}_{ij}})^{\frac{5}{2}} + (\overline{\mathcal{V}_{ij}} : \overline{\mathcal{V}_{ij}})^{\frac{5}{4}}} \quad (4)$$

in the above expression, $\overline{\mathcal{V}_{ij}}$ is the deviatoric part of the square of the velocity gradient tensor $\overline{\mathcal{V}_{ij}} = \frac{1}{2}\left(g_{ij}^2 + g_{ji}^2\right) - \frac{1}{3}\delta_{ij} g_{kk}^2$ with $g_{ij}^2 = g_{ik} g_{kj}$ and $\mathcal{C}_w$ is the model constant. Here a value of $\mathcal{C}_w = 0.325$ is used.

The governing equations are discretised on a collocated unstructured grid arrangement by means of second-order spectrum-consistent schemes (Verstappen and Veldman, 2003). Such schemes are conservative, i.e. they preserve the symmetry properties of the continuous differential operators and, ensure both stability and conservation of the kinetic-energy balance even at high Reynolds numbers and with coarse grids. For the temporal discretisation of the momentum equation a two-step linear explicit scheme on a fractional-step method is used for the convective and diffusive terms (Trias and Lehmkuhl, 2011), while for the pressure gradient term an implicit first-order scheme is implemented. For more details the user is referred to Rodríguez et al. (2011); Jofre et al. (2014); Trias et al. (2014) .

Definition of the case and boundary conditions

The flow past a circular cylinder at critical and super-critical Reynolds numbers in the range of $Re = U_{ref}\, D/\nu = 2.5 \times 10^5 - 8.5 \times 10^5$ is considered. The Reynolds number is defined in terms of the free-stream velocity U_{ref} and the cylinder diameter D. The cases are solved in a computational domain of dimensions $x \equiv [-16D, 16D]$; $y \equiv [-10D, 10D]$ for the stream- and cross-stream directions, whereas for the span-wise direction $z \equiv [0, 0.5\pi D]$ is considered for Reynolds number up to $Re = 6.5 \times 10^5$ and $z \equiv [0, D]$ for the higher Reynolds numbers. For all the cases the circular cylinder is placed at $(x, y, z) \equiv (0, 0, 0)$.

Table 1: Computational meshes NCV_t total number of CVs; $N_{CV\ plane}$ number of CVs in the plane; N_{planes} number of planes in the span-wise direction

Re	NCV_t [MCVs]	$N_{CV\ plane}$	N_{planes}
2.5×10^5	38.4	299683	128
3.8×10^5	48.6	379950	128
5.3×10^5	64.1	500516	128
6.5×10^5	83.2	650432	128
7.2×10^5	89.4	698949	128
8.5×10^5	105.1	820803	128

The boundary conditions consist of uniform velocity (u,v,w)=(1,0,0) at the inflow, slip conditions at the top and bottom boundaries of the domain, while at the outlet a pressure-based condition is used. At the cylinder surface, no-slip conditions are prescribed. As for the span-wise direction, periodic boundary conditions are imposed.

Different grids up to ~ 105 million CVs are used, depending on the Reynolds number. The boundary layer at the cylinder surface is well resolved, i.e. no wall function is used. Thus, the meshes are designed so as to keep the non-dimensional wall distance $y^+ \leq 2$. To do this, a prism layer is constructed around the cylinder surface. In the problem here considered, transition to turbulence occurs in the boundary layer. Thus, it should be stressed that in the present formulation transition to turbulence is well captured by the model, i.e. no artificial mechanism is imposed for triggering this phenomenon to occur. Details about the grids used are given in table 1.

3 Results

Figure 1 depicts the total drag coefficient and the pressure distribution on the cylinder surface at different Reynolds numbers compared with experimental results from the literature. At these Reynolds numbers, there is a large scattering in the measurements, as this quantity is highly affected by the cylinder surface roughness, wind tunnel blockage ratio, inlet conditions, among other issues. It should be considered that in these experiments Reynolds number increments are carried out by small increments of the wind tunnel speed Schewe (1983). Under these circumstances, the measurements might be influenced by the previous state. Moreover, as it was also pointed out by Schewe (1983), fluctuations in the transition states (when the

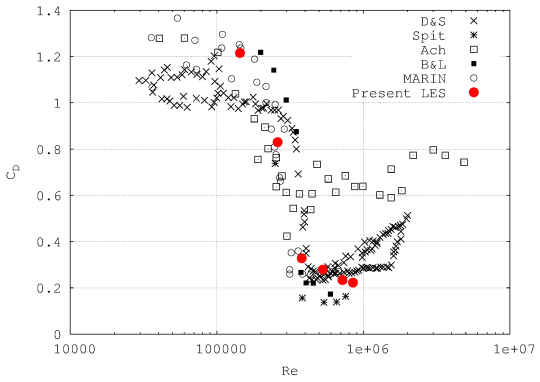

(a)

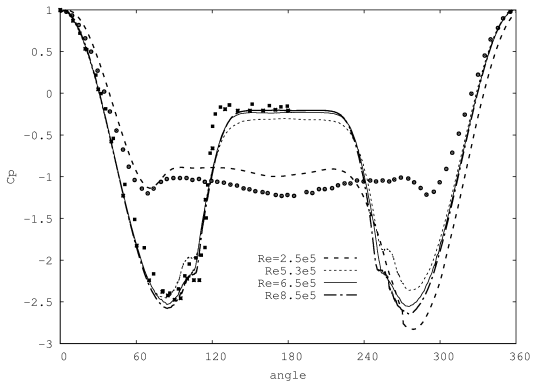

(b)

Figure 1: (a)Drag coefficient vs. Reynolds number. (b) Local pressure distribution at different Reynolds numbers. Comparison with the literature. (circles) Cantwell and Coles (1983) $Re = 1.4 \times 10^5$, (stars) Bursnall and Loftin (1951) $Re = 5.96 \times 10^5$, (solid squares) Flaschbart (taken from Roshko (1961))

one-bubble flow was detected) were the largest and the wind tunnel speed was influenced by the transition states, as far as the drag changes in the cylinder were not small enough compared with the drag of the tunnel. Similar issues were also reported by Shih et al. (1993). Nonetheless, there is a reasonable agreement between numerical and experimental results for the whole range of Reynolds numbers here considered.

One noticeable feature is the depression which occurs on one-side of the cylinder at $Re = 2.5 \times 10^5$, the pressure profile is asymmetric, pointing out that boundary layer separation and transition to turbulence occurs at different locations on the top and bottom sides of the cylinder, as it will be discussed hereafter. With the increase in the Reynolds number, the pressure distribution recovers its symmetry with a large depression on both sides of the cylinder. The main flow parameters are summarised in Table 2.

Critical regime

As commented before, at $Re = 2.5 \times 10^5$, pressure distribution is asymmetric. In fact, on one side of the cylinder, pressure minimum occurs near 70° and

Re	C_D	$-Cp_b$	$\varphi_{sep}[^\circ]$	St
2.5×10^5	0.83	0.99	91.5/217.7	0.238
3.8×10^5	0.481	0.48	145.2/218.8	0.238/0.358
5.3×10^5	0.296	0.305	148/212	0.368
6.5×10^5	0.232	0.23	148/212	0.442
7.2×10^5	0.231	0.225	148/212	0.449
8.5×10^5	0.222	0.206	148/212	0.456

Table 2: Flow parameters at different Re numbers. C_D drag coefficient, Cp_b base pressure, φ_{sep} separation angle (for the cases with LSB indicates the location of the first separation),φ_{Pmin} location where minimum pressure occurs, St vortex shedding frequency.

its distribution, similar to that observed in subcritical flows, comparing quite well with that obtained by Cantwell and Coles (1983) at the subcritical Reynolds number of $Re = 1.4 \times 10^5$ (see fig. 1b). While on the top side the flow behaviour is essentially as in the subcritical regime, the bottom side has undergone turbulent with the transition point closer to the cylinder surface, thus forming a larger depression. This causes the asymmetry observed and, as a consequence, a non-zero magnitude of the lift coefficient ($C_l > 0$). As transition to turbulence occurs close to the cylinder, Reynolds stresses make the separated boundary layer to reattach to the cylinder surface forming a small laminar separation bubble (LSB). This LSB, similar to that formed in the flow past aerodynamic profiles is here very small and thus, difficult to capture by means of numerical simulations. In fact, it is about 0.0038D at its center at $Re = 5.3 \times 10^5$ (see figure 2) and around 0.003D at $Re = 6.5 \times 10^5$. Indeed, in order to capture such tiny flow feature it has been necessary to design a quasi-DNS mesh near the cylinder surface. Further separation of the turbulent boundary layer occurs at a higher surface angle in the rear side (see table 2). The existence of asymmetries in the critical regime was also reported experimentally by Bearman (1969) and Schewe (1983).

With the increase in the Reynolds number, the small recirculation bubble appears on both sides of the cylinder and the symmetry in the forces is recovered as the drag approaches to its minimum value (see figure 1).As this happens, the location of the minimum pressure moves towards the rear while it gets more negative. At the same time, the base pressure rises, thus increasing the magnitude of the pressure gradient. With all these variations in the pressure distribution along the cylinder circumference, the drop in the drag up to ~ 0.23 in the critical regime is completed at the Reynolds number of $Re = 6.5 \times 10^5$.

The flow topology also registers major changes in the critical regime (see figures 3a,b and 4). In figure 3, coherent structures are represented by means of the second invariant of the velocity gradient tensor (Q-criterion by Hunt et al. (1988)). As can be seen, there

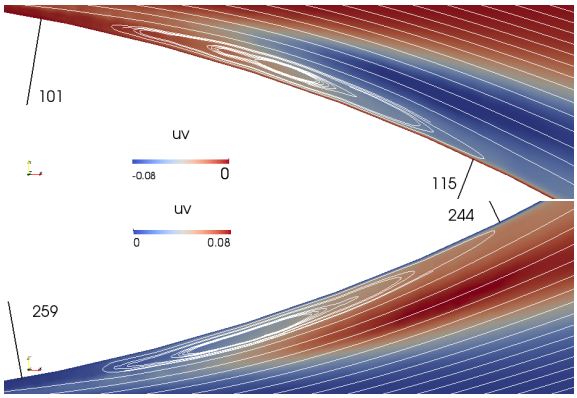

Figure 2: Close-up of the LSB region. Streamlines and shear-stresses at both sides of the cylinder surface at $Re = 5.3 \times 10^5$

is a reduction in the wake width and a variation in the location at which the boundary-layer separates. For instance, in figure 3a at $Re = 2.5 \times 10^5$, the asymmetry of the separation point can readily be seen. This behaviour is also observed in the mean flow as shown in figure 4. In the figure, mean streamlines in the near wake region are depicted for different Reynolds numbers. At $Re = 2.5 \times 10^5$, recirculation vortices are of different shape and streamlines are bent towards the upper part of the wake as a consequence of the difference in the magnitude of the forces acting on both sides of the cylinder. This effect is also present at $Re = 3.8 \times 10^5$ but in a lower degree. In this case, the wake is bent down and separation points occurs at different positions on both sides, pointing out an asymmetry in the forces at this Reynolds number.

Another important change in the wake in this regime is the shortening of the the stream-wise distance between the vortices in the wake as the Reynolds number increases. This occurs due to the increase in the vortex shedding frequency as it will be explained thereafter.

Super-critical regime

In this range, the flow is again almost symmetric as can be inferred from the pressure distribution profiles plotted in figure 1(b). The agreement with experimental results is also satisfactory. In fact, the present computations reproduce quite well the plateau in the pressure profile produced by a laminar separation bubble (LSB) which is formed around $\theta = 110°$ (measured from the front stagnation point). This small recirculation bubble anticipated by the experimental measurements is here well captured by the present computations.

Analysing the flow topology at these Reynolds numbers, it is quite different to that observed at critical and sub-critical Reynolds numbers (see figure 3c-d and 4). The wake width is lower than the cylinder diameter and average recirculation vortices although smaller are quasi-symmetric. In fact, in the super-

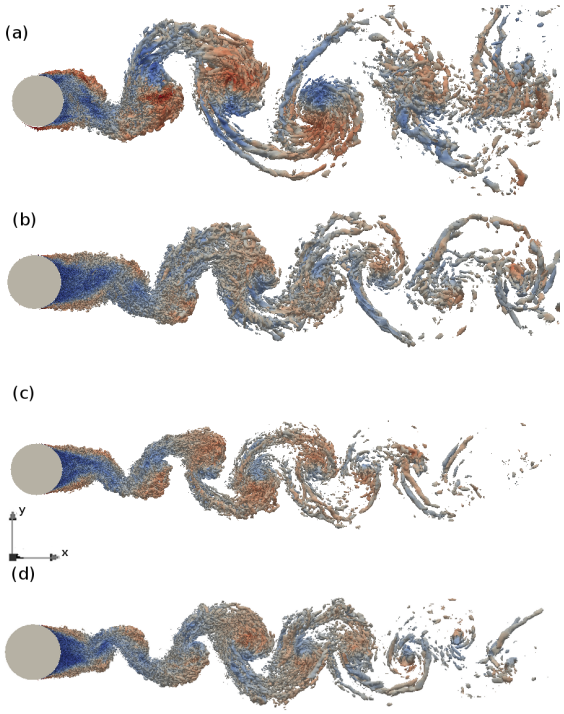

Figure 3: Instantaneous wake configuration. Vortical structures represented by isocountours of $\mathcal{Q} = 20$ coloured by the velocity magnitude (a) $Re = 2.5\times10^5$, (b) $Re = 5.3\times10^5$, (c) $Re = 6.5\times10^5$, (d) $Re = 8.5 \times 10^5$

critical regime, there are no major variations in the wake topology as can be observed when compared $Re = 6.5 \times 10^5$ and $Re = 8.5 \times 10^5$ in figure 3. Forces acting on the cylinder surface are now stabilized and the profiles of the pressure distribution are quite similar as also showed in figure 1(b).

It can also be observed that detached shear layers have collapsed around the cylinder centreline. However, due to the acceleration of the flow, both shear layers are brought closer each other and their interaction occur at a higher frequency. Thus, vortices shed at a regular frequency form a more compact von-Kármán-like vortex street (compared with sub-critical and critical regimes). These observations contrast with some experimental investigations (see for instance Shih et al. (1993)) as it is discussed hereafter.

Vortex shedding

There is little information about the vortex shedding in critical and supercritical regimes, contrary to the subcritical regime where consistent measurements of this quantity can be found in the literature (see for instance Williamson (1996)) and there is an agreement regarding an almost constant non-dimensional vortex shedding frequency of $St = fU/D =\sim 0.19 - 0.21$. At the Reynolds numbers here considered, values reported are quite scattered and inconsistency in the measurements are found (see figure 5). In fact, it has

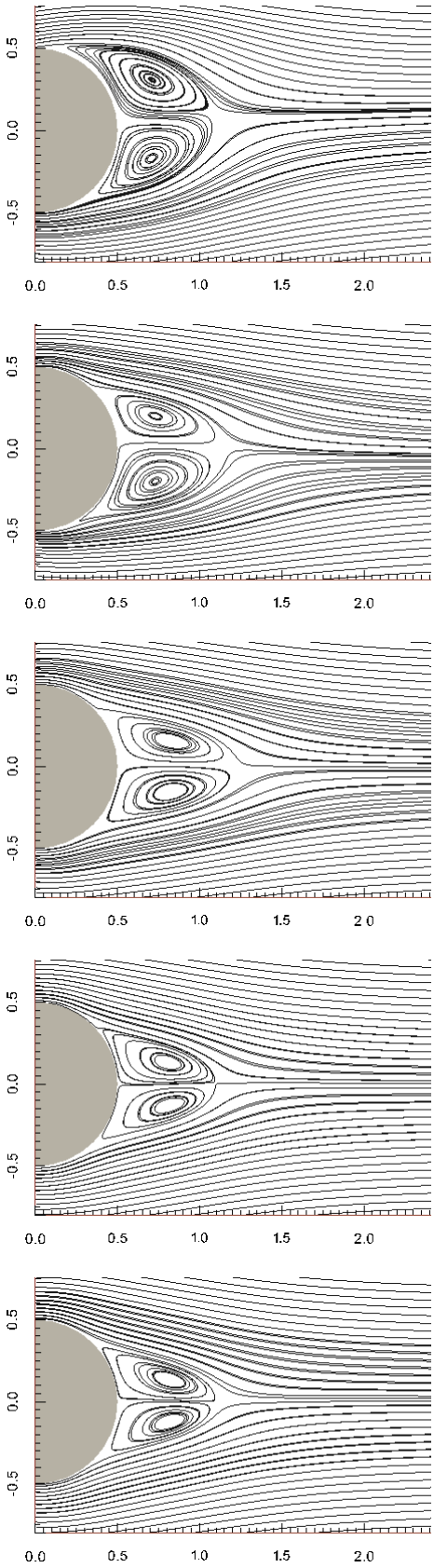

Figure 4: Mean streamlines. From top to bottom: $Re = 2.5 \times 10^5$; $Re = 3.8 \times 10^5$; $Re = 5.3 \times 10^5$; $Re = 6.5 \times 10^5$; $Re = 8.5 \times 10^5$;

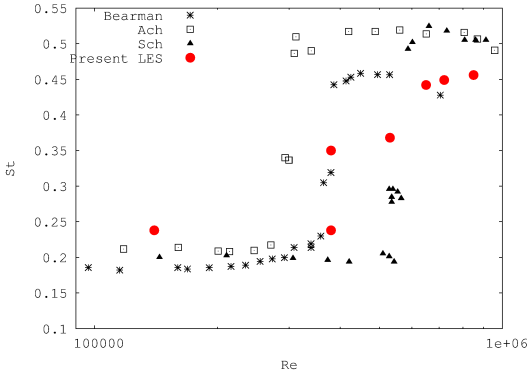

Figure 5: Non-dimensional vortex shedding frequency compared against results from the literature.

been argued that in the super-critical regime vortex shedding ceases to occur (see for instance Shih et al. (1993)). However, in the present computations vortex shedding does occur at every Reynolds number as can be seen from the energy spectrum shown in figure 6 and a von Kármn vortex street is observed (see figure 3). The energy spectra depicted in figure 6 correspond with the spectra of the cross-stream velocity fluctuations for a probe located at $[x, y] \equiv [2D, 0.5D]$ regardless the Reynolds number. The energy spectra have been calculated by using the Lomb periodogram technique and the resulting spectra have also been averaged in the homogeneous direction. As can be seen, vortex shedding peak is displaced towards higher frequencies as the Reynolds number increases in the critical regime. Indeed, at $Re = 2.5 \times 10^5$ vortex shedding frequency is 0.235. At $Re = 3.8 \times 10^5$ two small peaks in the spectrum are measured at frequencies of 0.238 and 0.35, whereas at $Re = 5.3 \times 10^5$ it is 0.36, to then rise again up to $\sim$0.45 in the supercritical zone. This value is then kept almost constant for al the supercritical range. In spite of the scattering in the few measurements of the vortex shedding at these Reynolds numbers, the values obtained are in quite good agreement with those reported in the literature Bearman (1969); Achenbach and Heinecke (1981) as shown in figure 5.

Comparing the changes in the wake topology with those in the fundamental frequency, it is clear that both variations are closely related. As the shear layers come closer due to the acceleration of the flow, their interaction is promoted and thus, the periodic vortex shedding takes place at a higher frequency (see table 2).

The reason why some investigators did not detect vortex shedding at $Re > 4 \times 10^5$ is not fully clear (see for instance Roshko (1961); Van Nunen (1974); Shih et al. (1993)). However, at these Reynolds numbers the flow is quite unstable and aspects such as a low cylinder aspect ratio or vibrations in the wind tunnel can trigger three-dimensional effects in the wake and the loss of coherence in the vortex shedding. Indeed, Achenbach and Heinecke (1981) observed these effects for low aspect ratio cylinders and under those

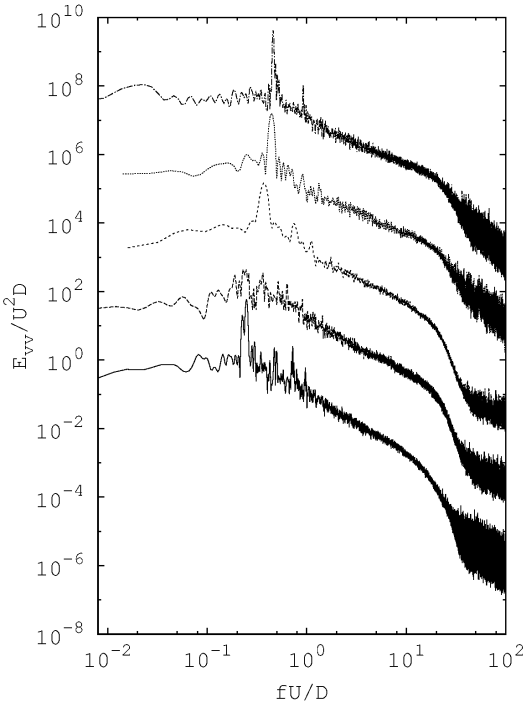

Figure 6: Energy spectra of velocity fluctuations at $[x, y] \equiv [2D, 0.5D]$ at different Reynolds numbers. From bottom to top: $Re = 2.5 \times 10^5$; $Re = 3.8 \times 10^5$; $Re = 5.3 \times 10^5$; $Re = 6.5 \times 10^5$; $Re = 8.5 \times 10^5$ (for clearness energy spectra are shifted except that at $Re = 2.5 \times 10^5$)

circumstances no regular signal was detected. These effects disappeared when cylinders of larger aspect ratio were used. It would be then interesting to induce some three dimensional effects in order to clarify this issue. However, at this time this remains a subject for further research.

4 Conclusions

Large eddy simulations of the flow past a circular cylinder at critical and super-critical regime have been carried out. Results for the drag coefficient and pressure distribution agree well with experimental measurements. At these Reynolds the wake suffers a topological change with the final collapse of the shear layers in the wake centreline. In spite of the changes taking place at these Reynolds numbers, the shed of coherent vortices is well detected, but the frequency at which they are shed rose from 0.238 at the upper part of the critical regime to 0.45 in the super-critical regime.

Acknowledgments

This work has been financially supported by the Ministerio de Economía y Competitividad, Secretaría de Estado de Investigación, Desarrollo e Innovación, Spain (Ref. ENE2010-17801) and, by the Collaboration Project between Universitat Politècnica de Catalunya and Termo Fluids S.L. We acknowledge PRACE for awarding us access to resource MareNostrum III based in Barcelona, Spain. We also acknowledge the technical expertise, assistance and access to MareNostrum II provided by the Red Española de Supercomputación.

References

Achenbach E. 1968 *J. Fluid Mech* **34**, 625–639.

Achenbach E. and Heinecke E. 1981 *J. Fluid Mech* **109**, 239–251.

Bearman P. 1969 *J. Fluid Mech* **37**, 577–585.

Bearman P. W. 1965 *Journal of Fluid Mechanics* **21**, 241–255.

Breuer M. 2000 *International Journal of Heat and Fluid Flow* **21**(5), 648–654.

Bursnall W. and Loftin L. J. 1951 Experimental investigation of the pressure distribution about a yawed circular cylinder in the critical Reynolds number range Technical Report NACA TN2463 NACA.

Cantwell B. and Coles D 1983 *Journal of Fluid Mechanics* **136**, 321–374.

Catalano P., Wang M., Iaccarino G. and Moin P. 2003 *International Journal of Heat and Fluid Flow* **24**(4), 463–469.

Delany N. and Sorensen N. 1953 Low-speed drag of cylinders of various shapes Technical Report NACA TN3038 NACA.

Dong S., Karniadakis G. E., Ekmekci A. and Rockwell D. 2006 *Journal of Fluid Mechanics* **569**, 185.

Hunt J., Wray A. and Moin P. 1988 Eddies, stream and convergence zones in turbulent flows Technical Report CTR-S88 Center for turbulent research.

Jofre L., Lehmkuhl O., Ventosa J., Trias F. X. and Oliva A 2014 *Numerical Heat Transfer, Part B: Fundamentals* **54**(1), 53–79.

Lehmkuhl O., Rodríguez I., Borrell R. and Oliva A. 2013 *Physics of Fluids* **25**, 085109.

Moussaed C., Vittoria Salvetti M., Wornom S., Koobus B. and Dervieux A. 2014 *Journal of Fluids and Structures* pp. 1–10.

Nicoud F. and Ducros F. 1999 *Flow, Turbulence and Combustion* **62**, 183–200.

Rodríguez I., Borrell R., Lehmkuhl O., Pérez-Segarra C. and Oliva A. 2011 *Journal of Fluid Mechanics* **679**, 263–287.

Roshko A. 1961 *Journal of Fluid Mechanics* **10**(03), 345–356.

Schewe G. 1983 *Journal of Fluid Mechanics* **133**, 265–285.

Shih W., Wang C., Coles D. and Roshko A. 1993 *Journal of Wind Engineering and ...* **49**, 351–368.

Trias F.X. and Lehmkuhl O. 2011 *Numerical Heat Transfer. Part B* **60**(2), 116–134.

Trias F.X., Lehmkuhl O., Oliva A, Pérez-Segarra C. and Verstappen R. 2014 *Journal of Computational Physics* **258**, 246–267.

Van Nunen J. 1974 *in* Springer-Verlag, ed., 'Flow Induced Structural Vibrations' Berlin pp. 748–754.

Verstappen R. W. C. P. and Veldman A. E. P. 2003 *Journal of Computational Physics* **187**, 343–368.

Williamson C. H. K. 1996 *Annual Review of Fluid Mechanics* **28**(1), 477–539.